Nanoscale phosphoinositide distribution on cell membranes of mouse cerebellar neurons

Authors

Kohgaku Eguchi[1*] and Ryuichi Shigemoto[1*]

[1]Institute of Science and Technology Austria (ISTA), Am Campus 1, 3400 Klosterneuburg, Austria

[*]For correspondence: kohgaku.eguchi@ist.ac.at (KE); ryuichi.shigemoto@ist.ac.at (RS)

Abstract

Phosphatidylinositol-4,5-bisphosphate (PI(4,5)P_2) plays an essential role in neuronal activities through interaction with various proteins involved in signaling at membranes. However, the distribution pattern of PI(4,5)P_2 and the co-clustering with these proteins on the neuronal cell membranes remain elusive at the electron microscopic level. In this study, we quantitatively investigated the nanoscale distribution of PI(4,5)P_2 on the neuronal cell membranes by SDS-digested freeze-fracture replica labeling with cryo-fixed mouse cerebellum. We demonstrate that PI(4,5)P_2 makes clusters with a mean size of ~ 1,000 nm^2 and these clusters show preferential accumulation in specific membrane compartments depending on cell types. Purkinje cell (PC) spines and granule cell (GC) presynaptic active zones are particularly rich in the PI(4,5)P_2 clusters. Furthermore, these clusters are extensively associated with clusters of $Ca_V2.1$ and GIRK3 throughout different membrane compartments of PCs, GCs, and molecular layer interneurons. In contrast, these clusters showed compartment-specific association with mGluR1α in PC spines. These results suggest that visualization of the nanoscale PI(4,5)P_2 distribution may provide insight into the physiological functions of PI(4,5)P_2 in neurons.

Introduction

Phosphoinositides (PIs) are minor components on the cytoplasmic side of eukaryotic cell membranes, but they play essential roles in a wide variety of cellular functions. In neuronal cells, each stereoisomer of PIs is distributed in different subcellular compartments (Haucke, 2005; Idevall-Hagren and De Camilli, 2015; Wenk and De Camilli, 2004): PI(4)P is enriched in the membrane of the Golgi apparatus and synaptic vesicles (SVs), PI(4,5)P_2 and PI(3,4,5)P_3 mainly exist in the plasma membrane, PI(3)P and PI(3,5)P_2 are selectively concentrated on early and late endosomes, respectively. PIs contribute to various aspects of neuronal activity, such as synaptic transmission and maintenance of membrane excitability by regulating ion channels and intracellular signaling pathways. At chemical synapses, PIs regulate exo- and endocytosis of synaptic vesicles at the presynaptic sites (Lei et al., 2017; Martin, 2001; Posor et al., 2015; Ueda and Hayashi, 2013)Many proteins related to SV exo- and endocytosis have binding domains to one or several stereoisomers of PIs (Di Paolo and De Camilli, 2006; Falkenburger et al., 2010), indicating a potential role of PIs as an anchor for these presynaptic proteins to regulate their localization and dynamics during synaptic transmission. At the postsynaptic sites, PIs regulate the morphological plasticity of dendritic spines through actin remodeling (Lei et al., 2017; Martin, 2001; Posor et al., 2015; Ueda and Hayashi, 2013)during long-term potentiation (Lei et al., 2017; Martin, 2001; Posor et al., 2015; Ueda and Hayashi, 2013).

Although it is essential to know the distribution pattern of PIs and their association with signaling proteins at neuronal cell membranes to understand the roles of PIs in neuronal activities, it has been poorly investigated due to several technical issues in the conventional methods (Tsuji et al., 2019). Immunoelectron microscopy using anti-PI(4,5)P_2 antibody allows for observing the nanoscale PI(4,5)P_2 distribution on the cell membrane, but the use of aldehyde-fixed cell preparations has a potential issue because aldehydes cannot fix the lateral diffusion of most membrane lipids across the membrane (Tanaka et al., 2010). Fluorescent probes for PIs based on a PI-binding domain (PBD) of proteins have been developed to visualize PIs in living cells (Idevall-Hagren and De Camilli, 2015; Maekawa and Fairn, 2014). However, this method does not have sufficient spatial resolution to observe the nanoscale distribution of PIs in small compartments in neuronal cell membranes, such as presynaptic active zones (AZs) and postsynaptic densities (PSDs). In addition, the overexpressed PBD-based probes mask PIs and competitively interfere with their interactions

with proteins in the living cells (Suh and Hille, 2008).

To solve these issues and visualize the nanoscale distribution of PIs on cell membranes, sodium dodecyl sulfate-digested freeze-fracture replica labeling (SDS-FRL) combined with cryofixation has been utilized (Aktar et al., 2017; Cheng et al., 2014; Fujita et al., 2009; Ozato-Sakurai et al., 2011; Tsuji et al., 2019). This immunoelectron microscopic method enables nanoscale membrane phospholipid labeling by physically fixing membrane molecules without chemical fixation. In this study, we optimized this SDS-FRL method to acute mouse cerebellar slices and investigated the nanoscale distribution of PI(4,5)P_2 on neuronal cell membranes using recombinant GST-tagged pleckstrin homology (PH) domain of phospholipase Cδ1 (PLCδ1) as a specific probe for PI(4,5)P_2. This approach allowed us to quantitatively examine the numbers, densities, and distribution patterns of PI(4,5)P_2 on somatodendritic and axonal membranes, including post- and presynaptic sites in mouse cerebellar neurons. We show that PI(4,5)P_2 makes small clusters on neuronal membranes and specifically co-clusters with P/Q-type voltage-gated calcium channels, G-protein-coupled inwardly rectifying potassium channels, and metabotropic glutamate receptors in distinct membrane compartments, giving insights into the physiological functions of PI(4,5)P_2 in the regulation of neuronal excitability and neurotransmitter release.

Results

Visualization of nanoscale PI(4,5)P_2 distribution on SDS-digested freeze-fracture replica preparations of mouse brain tissues

To observe the nanoscale two-dimensional distribution of PI(4,5)P_2, SDS-FRL has been utilized on cultured human fibroblasts, mouse smooth muscle cells, and rat pancreatic exocrine acinar cells (Fujita et al., 2009; Ozato-Sakurai et al., 2011). In this study, we optimized this method for mouse cerebellar tissues to quantitatively analyze the nanoscale PI(4,5)P_2 distribution on neuronal cell membranes. We used a recombinant GST-tagged PH domain of PLCδ1 (GST-PH) as a specific probe of PI(4,5)P_2. To verify the specificity of GST-PH among the PI stereoisomers, we labeled freeze-fracture replicas of liposomes containing either PhdIns or a PI stereoisomer (5 mol%) with GST-PH (50 ng/ml), anti-GST primary antibody, and gold particle-conjugated secondary antibody. The density of

immunogold particles was much higher on the replica prepared from PI(4,5)P_2 liposome compared to those from other liposomes (Figure 1A), indicating a high specificity of the PI(4,5)P_2 probe (Figure 1B).

To visualize the two-dimensional (2D) distribution of PI(4,5)P_2 on neuronal cell membranes, we labeled PI(4,5)P_2 in the mouse cerebellum using SDS-FRL with GST-PH. Acute slices prepared at physiological temperature (Eguchi et al., 2020) were frozen under high pressure with 15% PVP as a cryoprotectant (Figure 1C) to minimize damage caused by ice crystals during freezing (Borges-Merjane et al., 2020). After the SDS-digestion to remove cytosolic proteins and extracellular matrix, cerebellar replicas were sequentially incubated with GST-PH, primary antibodies, and gold particle-conjugated secondary antibodies. $Ca_V2.1$ was co-labeled using an anti-$Ca_V2.1$ antibody directed against its intracellular domain (Althof et al., 2015), giving specific labeling on the cytoplasmic leaflets (P-face) of neuronal cell membranes. Immunogold particles that label PI(4,5)P_2 by GST-PH (PI(4,5)P_2 particles) showed higher density on the P-face of the somatic membrane of Purkinje cells (PCs) than on the E-face (Chi-square likelihood-ratio test (Chi-LRT): $p < 0.001$; Figures 1D and 1E), indicating the dominance of PI(4,5)P_2 distribution on the cytoplasmic leaflet of the cell membranes. The particle density without GST-PH was significantly lower on both E- and P-face of the PC somatic membranes than that with GST-PH (Figures S1A and S1B), indicating that even the low-density PI(4,5)P_2 labeling on the E-face is ascribable to GST-PH binding.

To quantitatively investigate whether PI(4,5)P_2 is clustered on somatic membranes of PCs, we performed Monte-Caro random simulations and compared the nearest neighbor distance (NND) between the observed and simulated PI(4,5)P_2 particles from all images (Szoboszlay et al., 2017). The mean NNDs of the observed PI(4,5)P_2 particles were around half of the simulated one (Chi-LRT: $p < 0.001$, Figure 1F), indicating clustering of PI(4,5)P_2 on the membrane. The distribution of NNDs between PI(4,5)P_2 particles obtained from a PC somatic membrane (Figure 1G) is highly right-skewed (skewness = 3.55). Fitting this distribution with Gaussian mixture modeling shows that the NNDs between PI(4,5)P_2 particles are produced from a mixture of short and long NND populations. These results indicate that PI(4,5)P_2 on the PC soma has two distinct distribution patterns, clustered and scattered, and that most PI(4,5)P_2 constitute clusters (Figure 1G). The PI(4,5)P_2 particle clusters were also observed on the E-face of the somatic membrane (Figure S1C). The number of particles in a cluster was significantly lower without GST-PH than that with GST-PH on both E- and P-face (Figure S1C). These results indicate that PI(4,5)P_2 forms clusters on both the outer and

123 inner leaflets of the somatic membranes.

124 To examine whether the density of $PI(4,5)P_2$ differs between neuronal cell types in the
125 cerebellum, we observed somatic membranes of cerebellar granule cells (GCs) and molecular
126 layer interneurons (MLIs). $PI(4,5)P_2$ particles were also distributed on the P-face making
127 clusters in somatic membranes of both cell types (Figure 1H). Although the density of
128 $PI(4,5)P_2$ particles in the somatic membrane of GCs was significantly higher than that of
129 MLIs (multiple pairwise comparisons with Tukey adjustment (Tukey): $p < 0.001$; Figure 1I),
130 the NNDs of the $PI(4,5)P_2$ particles on somatic membranes of the cerebellar neurons did not
131 differ between the cell types (Chi-LRT: $p = 0.12$; Figure 1J), indicating a similar local
132 concentration of $PI(4,5)P_2$ in these clusters across the examined cerebellar neuronal cell
133 types.

134

135 **$PI(4,5)P_2$ distribution on somatodendritic compartments of PCs**

136 We next investigate whether the distribution of $PI(4,5)P_2$ differs among somatodendritic
137 compartments of PCs: somata, main shafts (MS), smooth branchlets (SmB), spiny branchlets
138 (SpB), and spines. EM pictures of each dendritic component were taken in the molecular
139 layer (ML) divided into proximal (MS), intermediate (SmB) and distal one-third (SpB,
140 spines) of the PC layer. Gold particles for $PI(4,5)P_2$ were observed throughout all the
141 dendritic compartments (Figure 2A). The density of $PI(4,5)P_2$ particles was found to increase
142 gradually from the proximal to the distal dendrites (Chi-LRT: $p < 0.001$; Figure 2B): spine
143 membranes showed a ~1.5 times higher density of $PI(4,5)P_2$ particles than somatic, MS, and
144 SmB membranes (Tukey: $p < 0.001$), whereas no significant difference compared to SpB
145 membranes was detected (Tukey: $p = 0.43$). Mean NNDs of $PI(4,5)P_2$ particles were not
146 significantly different between the compartments (Figure 2B, Chi-LRT: $p = 0.55$), indicating
147 that the local concentration of $PI(4,5)P_2$ does not differ between different somatodendritic
148 compartments of PCs.

149 $PI(4,5)P_2$ particles on the dendritic membranes formed clusters as seen on the somatic
150 membranes. To quantitatively compare the $PI(4,5)P_2$ cluster profiles (cluster area, particle
151 number in cluster, and intra-cluster density) between all compartments of somatodendritic
152 membranes, we detected the clusters using the Density-Based Spatial Clustering of
153 Applications with Noise (DBSCAN) algorithm (Methods, (Szoboszlay et al., 2017). The

154 DBSCAN detected variable sizes of PI(4,5)P_2 particle clusters on the somatodendritic
155 membranes (Figure 2C). The density of PI(4,5)P_2 clusters on the PC cell membranes
156 gradually increased from the proximal to the distal compartments (Chi-LRT: $p < 0.001$;
157 Figure 2D); spine membranes showed a higher density of PI(4,5)P_2 clusters than somatic,
158 MS, and SmB membranes (Tukey: $p < 0.001$), whereas no significant difference with SpB
159 membranes was detected (Tukey: $p = 0.21$). The cluster area was not significantly different
160 between all compartments of somatodendritic membranes (Chi-LRT: $p = 0.10$; Figure 2D),
161 whereas intra-cluster PI(4,5)P_2 particle density in spines was significantly higher than those
162 in other compartments (Chi-LRT: $p < 0.001$; Figure 2D). These results suggest that PI(4,5)P_2
163 are distributed throughout all compartments of somatodendritic membranes of PCs, and the
164 density is higher at the distal dendrites and spines than at the soma and proximal dendrites.
165 This proximo-distal gradient of PI(4,5)P_2 along the somatodendritic compartments of PC
166 membranes is ascribable to an increase in the density of PI(4,5)P_2 clusters rather than the
167 cluster size, and a higher PI(4,5)P_2 density within clusters on spine membranes.

168

169 **PI(4,5)P_2 distribution on membrane compartments of GCs and MLIs**

170 We next examined the PI(4,5)P_2 distributions in different compartments of GCs (somata,
171 dendrites, parallel fiber (PF) axons, presynaptic PF boutons with PC spines (PF-PC) or MLI
172 dendrites (PF-MLI)) and MLIs (somata, dendrites, presynaptic basket cell boutons on PC
173 somata (BC-PC)). Gold particles for PI(4,5)P_2 were observed throughout all compartments of
174 GCs and MLIs (Figures 3A and 3B). In the GC membranes, the density of PI(4,5)P_2 particles
175 was not significantly different between the compartments (Chi-LRT: $p = 0.095$; Figure 3C),
176 though the mean NNDs of PI(4,5)P_2 particles were slightly but significantly different
177 between somatic and axonal membranes (Tukey: $p = 0.027$, Figure 3C). The cluster
178 parameters of PI(4,5)P_2 were also not significantly different between the compartments
179 (Figure 3D). These results suggest that PI(4,5)P_2 in GC membranes shows a similar
180 distribution pattern throughout the subcellular compartments.

181 In MLIs, the PI(4,5)P_2 density was not significantly different between the membrane
182 compartments, but the mean NNDs were larger in dendritic and presynaptic bouton
183 membranes than in somatic membranes (Figure 3E). This difference is caused by larger
184 population of scattered PI(4,5)P_2 in these compartments as shown in Figure S2. The intra-

185 cluster density of $PI(4,5)P_2$ in the bouton membrane was significantly higher than in the
186 somatic membrane, whereas the cluster density and area were similar between the
187 compartments (Figure 3F).

188

189 **$PI(4,5)P_2$ distribution on synaptic membranes**

190 Next, we focused on $PI(4,5)P_2$ distribution in the presynaptic membrane of PF (Figure 4A).
191 Since many presynaptic proteins related to neurotransmitter release contain $PI(4,5)P_2$-binding
192 domains (Martin, 2001), $PI(4,5)P_2$ is expected to be localized at the presynaptic active zones
193 (AZs). The $PI(4,5)P_2$ particle density was significantly higher in the AZs than in the whole
194 bouton and extra-AZ membranes at both PF-PC and PF-MLI synapses (Tukey: $p < 0.001$;
195 Figure 4B). The observed density of $PI(4,5)P_2$ particles in AZs was significantly higher than
196 that of randomly distributed $PI(4,5)P_2$ particles on the bouton membrane by Monte-Carlo
197 simulation (Chi-LRT: $p < 0.001$ (PF-PC) and $p = 0.002$ (PF-MLI); Figure 4C). Next, we
198 examined how the $PI(4,5)P_2$ particles are distributed within the AZs using the center-
199 periphery index (CPI), where a CPI of 0 indicates that the particle is at the center of gravity,
200 and a CPI of 1 indicates the particle is at the edge of the AZ (Kleindienst et al., 2020). The
201 histogram of CPI in the bouton membranes suggests that the particles are distributed at a high
202 density within the AZ and that the distribution probability decreases with distance from the
203 AZ (Figure 4D, top). The CPI of the particles within AZs was higher at around CPI = 1.0
204 compared to the values of the random simulation (Figure 4D, bottom), indicating that
205 $PI(4,5)P_2$ is preferentially located in the periphery of the AZs. The mean CPI of the $PI(4,5)P_2$
206 particles in AZs was significantly higher than that of randomly distributed particles (Chi-
207 LRT: $p < 0.001$, Figure 4E) in both PF-PC and PF-MLI synapses. These results suggest that
208 AZ, in particular, its periphery is $PI(4,5)P_2$-enriched regardless of postsynaptic cell types.

209 Next, we investigated the $PI(4,5)P_2$ distribution in PSD of dendritic spines. The $PI(4,5)P_2$
210 particles were distributed throughout the spine membranes (Figure 4F), and the density in the
211 PSDs was not significantly different compared to the whole spine and extra-PSD membranes
212 (Chi-LRT: $p = 0.77$; Figure 4G). The observed $PI(4,5)P_2$ particle density in PSDs was not
213 significantly higher than that of the particles randomly distributed in the spine (Chi-LRT: $p =$
214 0.25; Figure 4H). Furthermore, the CPI of the $PI(4,5)P_2$ particles in the spines was uniformly
215 distributed, and the CPI in the PSDs was similar to the simulated particles randomly

216 distributed (Figure 4I). These results suggest that PI(4,5)P_2 is not specifically accumulated in
217 the postsynaptic site of PC dendritic spines.

218

219 **The association of ion channels and receptors with PI(4,5)P_2 on cell membranes of**
220 **cerebellar neurons**

221 *The association of $Ca_V2.1$ with PI(4,5)P_2*

222 $Ca_V2.1$ is an α-subunit of P/Q-type voltage-gated calcium channels and is regulated by
223 PI(4,5)P_2 directly or indirectly through Ca_V β-subunit (Suh et al., 2012; Suh and Hille, 2008).
224 Here, we examined whether $Ca_V2.1$ is associated with PI(4,5)P_2 in the neuronal membranes
225 by co-immunolabeling of $Ca_V2.1$ with the PI(4,5)P_2 labeling. To assess the association, we
226 compared NNDs from $Ca_V2.1$ to PI(4,5)P_2 particles ($NND_{C\text{-}P}$) between observed and
227 simulated $Ca_V2.1$ particles. To reproduce the $Ca_V2.1$ clustering in the simulation, we
228 performed a fitted simulation of $Ca_V2.1$ particle distribution (Methods, (Kleindienst et al.,
229 2020; Luján et al., 2018b)). In PCs, $Ca_V2.1$ is broadly expressed in somatodendritic
230 membranes (Figure 5A) as previously reported (Indriati et al, 2013). The real values of
231 $NND_{C\text{-}P}$ in somatic, SpB, and spine membranes were significantly shorter than the simulated
232 ones (Figure 5B). The mean $NND_{C\text{-}P}$ was not significantly different between the
233 compartments of PC membranes (Figure 5C). In GCs, $Ca_V2.1$ was highly expressed in
234 somatic and presynaptic AZ membranes (Figure 5D). The comparison of $NND_{C\text{-}P}$ between
235 observed and simulated $Ca_V2.1$ particles showed significant differences in the somatic and
236 PF-PC/MLI AZ membranes (Figure 5E), indicating the association of $Ca_V2.1$ with PI(4,5)P_2.
237 The mean $NND_{C\text{-}P}$ values in PF-PC and PF-MLI AZs were not significantly different (Figure
238 5F). In MLI, $Ca_V2.1$ was expressed in somatic and presynaptic basket cell (BC)-PC bouton
239 membranes (Figure 6A). The $NND_{C\text{-}P}$ in somatic and BC-PC bouton membranes was
240 significantly shorter than the simulated one (Figure 6B). These results suggest the ubiquitous
241 association of $Ca_V2.1$ with PI(4,5)P_2 in neuronal cell membranes across various cell types
242 and their compartments.

243

244 *The association of GIRK3 channels with PI(4,5)P_2*

245 PI(4,5)P_2 is associated with some ion channels and regulates their activities, e.g., open
246 channel probability (Suh and Hille, 2008). G protein-coupled inwardly rectifying K^+ (GIRK)
247 channels are a family of lipid-gated potassium channels that are activated by PI(4,5)P_2 and G-
248 protein βγ-subunits ($G_{\beta\gamma}$) released from G-protein coupled receptors (GPCRs) (Whorton and
249 MacKinnon, 2011). Thus, GIRK channels are expected to be associated with PI(4,5)P_2
250 clusters in order to be efficiently activated. To examine whether PI(4,5)P_2 and GIRK
251 channels are co-clustered on dendritic membranes of mouse cerebellar PCs, we co-labeled
252 PI(4,5)P_2 and GIRK3, the most predominant subunit of GIRK channels in PCs (Aguado et al.,
253 2008; Fernández-Alacid et al., 2009), on the P-face of the dendritic membranes. The GIRK3
254 particles were observed throughout the dendritic SpBs and spines of the PCs (Figure 7A). We
255 compared the NNDs from GIRK3 to PI(4,5)P_2 particles ($NND_{G\text{-}P}$) between observed and
256 simulated GIRK3 particles in spines and SpBs spines of PCs. The real $NND_{G\text{-}P}$ in both spines
257 and SpBs was significantly shorter than the simulated one (Chi-LRT: $p < 0.001$, Figure 7B),
258 suggesting that GIRK3 channels co-clustered with PI(4,5)P_2 in the distal dendritic
259 membranes of PCs. GIRK channels are also expressed on presynaptic PF-PC boutons,
260 including AZs (Figure 7A, (Fernández-Alacid et al., 2009; Luján et al., 2018b), and may
261 regulate presynaptic excitability. In the presynaptic AZs, the real $NND_{G\text{-}P}$ was significantly
262 shorter than the simulated one (Chi-LRT: $p < 0.001$, Figure 7B), indicating the coexistence of
263 GIRK3 with PI(4,5)P_2. The mean $NND_{G\text{-}P}$ in spine and AZ membranes was significantly
264 shorter than that in SpB membranes (Figure 7C), suggesting the tighter association of GIRK3
265 and PI(4,5)P_2 in synaptic membranes.

266

267 *The association of mGluR1α with PI(4,5)P_2*

268 Group I metabotropic glutamate receptors (mGluRs) are GPCRs coupled with $G\alpha_q$ subunit
269 and hydrolyze PI(4,5)P_2 into inositol 1,4,5-trisphosphate (IP_3) and diacylglycerol (DAG)
270 through the activation of PLCβ. A subtype of Group I mGluRs mGluR1α is highly expressed
271 on the dendritic shafts and spines but avoids PSDs in PCs, and forms clusters (Luján et al.,
272 2018a). To effectively produce the second messengers from PI(4,5)P_2, a mGluR1α cluster is
273 expected to be located close to the PI(4,5)P_2 clusters on the dendritic membrane of PCs. To
274 address this possibility, we co-labeled mGluR1α with PI(4,5)P_2 on the dendritic membranes

275 of PCs and compared the NNDs between mGluR1α and PI(4,5)P_2 particles (NND_{M-P}) with
276 the fitted simulation of the mGluR1α particle distribution. The mGluR1α particles were
277 distributed as clusters on the membranes of spines and SpBs (Figure 7D-E) as previously
278 reported (Luján et al., 2018a). The real NND_{M-P} was significantly shorter than the simulated
279 one on the spine membrane (Chi-LRT: $p < 0.001$) but not on the SpB membrane (Chi-LRT: p
280 = 0.36, Figure 7F). These results suggest compartment-specific co-clustering of mGluR1α
281 with PI(4,5)P_2 on PC spines.

282

283 ## Discussion

284 ### Visualization of PI(4,5)P_2 distribution on neuronal cell membranes using SDS-FRL

285 To understand how and where PI(4,5)P_2 exerts the physiological functions in neurons, it is
286 essential to know its nanoscale distribution in the neuronal cell membranes. To visualize the
287 distribution of PI(4,5)P_2 on the cell membrane, cryofixation of phospholipids is necessary
288 because they diffuse laterally even after chemical fixation (Tanaka et al., 2010). Detergents
289 and organic solvents used in conventional immunoEM methods disrupt the cell membrane
290 and should be avoided. In regions with densely packed proteins such as AZs and PSDs,
291 limited accessibility of the probes could hamper quantitative analysis of the PI(4,5)P_2
292 distribution. The fluorescent protein-tagged PH domain of PLCδ1 has been developed as a
293 specific probe for PI(4,5)P_2 (Idevall-Hagren and De Camilli, 2015). This probe allows us to
294 perform single-molecule imaging of PI(4,5)P_2 on the plasma membrane of the cultured cells
295 using super-resolution microscopies such as Stimulated Emission Depletion (STED)
296 microscopy and Direct Stochastic Optical Reconstruction Microscopy (dSTORM)
297 (Milovanovic et al., 2016; Wang and Richards, 2012). However, it is still difficult to observe
298 the PI(4,5)P_2 distribution on neuronal cell membranes in brain tissues because of the limited
299 accessibility of the probes in AZs and PSDs. In addition, overexpressed fluorescent probes
300 interfere with endogenous protein binding to PI(4,5)P_2 by masking PI(4,5)P_2 on the cell
301 membrane (Suh and Hille, 2008), making it difficult to quantify the changes in PI(4,5)P_2.
302 Thus, the SDS-FRL with cryo-fixed brain tissue used in this study has the advantage of
303 visualizing accurately the native PI(4,5)P_2 distribution. In this method, phospholipids are
304 physically immobilized by high-pressure freezing and replication by deposition of evaporated
305 carbon/platinum, so the phospholipids do not diffuse after freezing. Since cytosolic proteins

306 are removed by SDS treatment, PI(4,5)P_2 and transmembrane proteins are exposed on the
307 replica surface, making high accessibility of the probes and antibodies. Due to a low temporal
308 resolution, it is still challenging to examine the dynamics of PI(4,5)P_2 during neuronal
309 activity, but it is a beneficial method to study the nanoscale distribution of PI(4,5)P_2 and
310 other phospholipids on neuronal cell membranes.

311 This study demonstrates that PI(4,5)P_2 is broadly distributed on neuronal cell membranes in
312 the mouse cerebellum. Comparisons of the PI(4,5)P_2 distribution between cell types revealed
313 slightly different densities of PI(4,5)P_2 particles on the somatic membrane, but the differences
314 in distribution patterns between subcellular compartments were more pronounced; in PCs, the
315 PI(4,5)P_2 density was higher at the distal dendrites than at the somatic and proximal
316 dendrites; in GCs, the density was similar at the somata, dendrites, axons, and presynaptic
317 boutons; in MLIs, the density of PI(4,5)P_2 in clusters was lower in presynaptic bouton
318 membranes than somatic and dendritic membranes. These differences in the PI(4,5)P_2
319 distribution patterns may reflect different roles of PI(4,5)P_2 in cell functions between
320 different cell types.

321

322 **PI(4,5)P_2 makes clusters on neuronal cell membranes in mouse cerebellum**

323 Previous studies using super-resolution microscopy have demonstrated that PI(4,5)P_2 forms
324 clusters of 50-100 nm in diameter on the cell membrane, as shown in PC12 cells (Aoyagi et
325 al., 2005; van den Bogaart et al., 2011; Wang and Richards, 2012) and mouse myoblast cells
326 (Petersen et al., 2016). Our study reveals that PI(4,5)P_2 forms clusters of around 1,000 nm^2
327 (corresponding to 35 nm in diameter) on the cell membrane of neurons in the acute cerebellar
328 tissues. The area of the clusters showed almost the same mean values in the somatodendritic
329 and axonal membranes of different neuronal cell types in the cerebellum. The cluster density
330 and the intra-cluster particle density of PI(4,5)P_2 in the PC spine membrane are higher than in
331 other somatodendritic compartments. These observations suggest the accumulation of
332 densely-packed PI(4,5)P_2 clusters in the spine membranes, supporting the contribution of
333 PI(4,5)P_2 and other PIs to spine formation and morphological long-term plasticity (Lei et al.,
334 2017; Ueda and Hayashi, 2013). Although it is still unknown why PI(4,5)P_2 forms clusters,
335 the clustered PI(4,5)P_2 localization indicates the importance of a close spatial relationship
336 between the clusters and effector proteins for their effective interaction, as discussed in the

337 following section.

338

339 **PI(4,5)P_2 distribution in the synaptic membrane**

340 In this study, we found the accumulation of PI(4,5)P_2 in AZ membranes of the presynaptic PF
341 boutons regardless of the postsynaptic cell types. This result suggests the roles of PI(4,5)P_2
342 on presynaptic activities, including vesicle exocytosis and endocytosis. At the presynaptic
343 membrane, Rab6-interacting proteins (RIMs) have PI(4,5)P_2-binding sites at C2A and C2B
344 domains, and their interactions are essential for efficient exocytosis (de Jong et al., 2018).
345 PI(4,5)P_2 also interacts with a SNARE protein syntaxin-1A and an SV Ca^{2+} sensor protein
346 synaptotagmin-1 (Aoyagi et al., 2005; Honigmann et al., 2013; Milovanovic et al., 2016).
347 Since $Ca_V2.1$ directly binds to RIMs and dominantly induces Ca^{2+} influx into PF boutons, the
348 association of $Ca_V2.1$ with PI(4,5)P_2 supports the idea that PI(4,5)P_2 anchors SVs and Ca^{2+}
349 channels through interaction with these proteins. PI(4,5)P_2 also regulates vesicle endocytosis
350 via interactions with endocytic proteins e.g., AP-2, AP180, clathrin, and dynamin (Haucke,
351 2005; Martin, 2001; Posor et al., 2015). At calyx of Held synapses of rat brainstem,
352 upregulation of PI(4,5)P_2 by the retrograde signals through the nitric oxide/cyclic GMP-
353 activated protein kinase/RhoA/Rho-associated protein kinase pathway accelerates vesicle
354 endocytosis, which strengthens the homeostatic plasticity for the maintenance of high-
355 frequency synaptic transmission (Eguchi et al., 2012; Taoufiq et al., 2013). PI(4,5)P_2 clusters
356 may work as anchors of presynaptic proteins involved in this pathway providing a site for
357 their interactions.

358

359 **Co-clustering of PI(4,5)P_2 and ion channels and receptors**

360 PI(4,5)P_2 regulates ion channels such as inwardly rectifying K^+ channels, KCNQ channels,
361 transient receptor potential (TRP) channels, and voltage-gated Ca^{2+} channels (Suh and Hille,
362 2008). Therefore, clarifying the distance relationship between these ion channels and
363 PI(4,5)P_2 may provide insight into the regulation mechanism of neuronal excitability by
364 PI(4,5)P_2. In this study, we found that GIRK3 was associated with PI(4,5)P_2 in SpB and
365 spines of PCs and also AZs of PF boutons. Because PI(4,5)P_2 is essential to activate GIRK
366 channels by βγ subunit of G protein (Whorton and MacKinnon, 2011), the association

367 between GIRK3 and PI(4,5)P_2 suggests that GIRK3 on SpB and spines is constantly ready to
368 be activated by G-protein coupled receptors. Since GIRK channels are also associated with
369 $GABA_B$ receptors at different compartments of the cerebellar neurons, such as dendritic
370 shafts and spines of PCs and AZs of PF boutons (Fernández-Alacid et al., 2009; Luján et al.,
371 2018b), the co-assembly of PI(4,5)P_2, GIRK channels and $GABA_B$ receptors may contribute
372 to effective inhibitory postsynaptic transmission on Purkinje cells (Luján et al., 2018b).

373 Group I mGluRs are GPCRs coupled with $G\alpha_q$ subunit and hydrolyze PI(4,5)P_2 into inositol
374 1,4,5-trisphosphate (IP_3) and diacylglycerol (DAG) through the activation of PLCβ. PCs
375 express mGluR1α, a subtype of Group I mGluRs, on the dendritic shafts and spines
376 concentrated in the peri-PSD areas (Luján et al., 2018a). We found a significant association
377 of mGluR1α with PI(4,5)P_2 clusters specific to the spine membrane in PCs, which may
378 contribute to the effective production of the second messengers from PI(4,5)P_2 in response to
379 the glutamate release from presynaptic PF boutons. On the other hand, no particular
380 concentration of PI(4,5)P_2 has been found in the peri-PSD areas. The diffusion dynamics of
381 PI(4,5)P_2 on the spine membrane may be enough to support the interaction with mGluR1α.
382 Thus, the tight spatial association of PI(4,5)P_2 as observed for $Ca_V2.1$ and GIRK3 may not be
383 necessary for the coupling of mGluR1α activation and intracellular signal cascade, though the
384 distance between mGluR1α (and the coupled PLCβ) and PI(4,5)P_2 may affect the kinetics of
385 the second messenger (IP_3 and DAG) production from PI(4,5)P_2.

386

387 The present study demonstrated that the SDS-FRL method could be successfully applied to
388 neuronal cells in acute mouse brain tissues to visualize the distribution of PI(4,5)P_2. We
389 quantitatively analyzed the nanoscale two-dimensional distribution of PI(4,5)P_2 on the cell
390 membrane of mouse cerebellar neurons, and its spatial relationship with GIRK3, $Ca_V2.1$, and
391 mGluR1α in PC dendrites and PF boutons. Notably, we have demonstrated a higher density
392 of PI(4,5)P_2 in distal PC dendrites, showing a specific association of mGluR1α with PI(4,5)P_2
393 in spines. PI(4,5)P_2 also showed concentration and association with $Ca_V2.1$ and GIRK3 in
394 presynaptic PF AZs. These results will help to elucidate the physiological functions of
395 PI(4,5)P_2 in neuronal activities, including SV fusion and retrieval in presynaptic membranes
396 and long-term plasticity in postsynaptic spine membranes. This method could also be a
397 powerful tool for the analysis of other PIs and phospholipid distribution in neuronal cell
398 membranes using specific probes.

399

400 # Materials and Methods

401 ## Animals

402 Animal experiments were conducted in accordance with the guideline of the Institute of
403 Science and Technology Austria (Animal license number: BMWFW-66.018/0012-
404 WF/V/3b/2016). Mice were initially purchased from Jackson Laboratory (Bar Harbor, ME,
405 USA) and were bred at the Preclinical Facility of IST Austria on 12:12 light-dark cycle with
406 access to food and water *ad libitum*. All experiments were performed in the light phase of the
407 cycle. C57BL/6J (stock number 000664) mice of either sex at postnatal (P) 5-7 weeks were
408 used in this study.

409

410 ## Liposome preparation and high-pressure freezing

411 Phosphatidylcholine (18:1 (Δ9-Cis) PC), phosphatidylethanolamine (18:1 (Δ9-Cis) PE),
412 phosphatidylserine (18:1 (Δ9-Cis) PS), phosphatidylinositol (18:1 PI) and phosphoinositides
413 (18:1) were from Avanti Polar Lipids. All liposomes contained 45 mol % PC, 30 mol % PE,
414 20 mol % PS, and either 5 mol % PI or a phosphoinositide. Solutions of PC, PE, and PS in
415 chloroform and PI or phosphoinositides in chloroform:methanol:H2O:HCl (1N) (20:9:1:0.1)
416 were mixed in the required proportion in amber-color glass vials. To improve
417 phosphoinositide homogenization with other lipids, the chloroform:methanol 2:1 ratio was
418 maintained in the mixture. A lipid film was produced by evaporation of solvents in the vial
419 under the stream of nitrogen gas and then drying using a vacuum desiccator for 2 h. The dried
420 lipid film was stored at -20 °C with argon gas and used within 2 days.

421 The lipid film was resuspended in a buffer containing 220 mM sucrose and 20 mM HEPES
422 (pH 7.4, adjusted with NaOH). The suspension was vortexed well and then freeze-thawed 5
423 times in liquid nitrogen and warm water (~60 °C). Unilamellar liposomes were produced by
424 extrusion through a 0.4 µm pore size polycarbonate filter using an extrusion apparatus
425 (Avanti Polar Lipids). After extrusion, the liposomes were diluted 5 times in 120 mM NaCl,
426 20 mM HEPES buffer (pH 7.4, adjusted with NaOH), and centrifuged for 20 min at 15,000 g.
427 The same amount of 100% glycerol was applied to the pellets of the liposomes as a

428 cryoprotectant. The liposome/glycerol mixture was placed on a copper carrier with a ring of
429 double-sided tape (140-µm thickness), covered with another carrier, and then frozen by a
430 high-pressure freezing machine (HPM010, BAL-TEC). The frozen samples were stored in
431 liquid nitrogen until use.

432

433 **High-pressure freezing of acute cerebellar slices**

434 Acute slices of mouse cerebellum were prepared at physiological temperature (PT) as
435 described previously (Eguchi et al., 2020). Briefly, mice were decapitated under isoflurane
436 anesthesia and their brains were quickly removed from the skull and immersed into a cutting
437 solution containing (mM): 300 sucrose, 2.5 KCl, 10 glucose, 1.25 NaH_2PO_4, 2 Na Pyruvate, 3
438 *myo*-inositol, 0.5 Na ascorbate, 26 $NaHCO_3$, 0.1 $CaCl_2$, 6 $MgCl_2$ (pH 7.4 when gassed with
439 95% O_2/5% CO_2) at PT (35-37 °C). The cerebellum was dissected from the whole brain and
440 immediately glued on a cutting stage of a tissue slicer (Linear Slicer Pro7, Dosaka EM,
441 Kyoto, Japan) and sliced (sagittal, 140-160 µm thickness) in the cutting solution kept at PT.
442 Slices were then maintained in the artificial cerebrospinal fluid (ACSF) containing (in mM):
443 125 NaCl, 2.5 KCl, 10 glucose, 1.25 NaH_2PO_4, 2 sodium pyruvate, 3 *myo*-inositol, 0.5
444 sodium ascorbate, 26 $NaHCO_3$, 2 $CaCl_2$, 1 $MgCl_2$ (pH 7.4 when gassed with 95% O_2/5%
445 CO_2) at 37 °C until use. Small blocks containing lobule IV-VII were trimmed from the slices
446 in the cutting solution using a micro scalpel (#10316-14, FST). The trimmed block was
447 transferred into cryoprotectant buffer (15% polyvinylpyrrolidone in ACSF with 10 mM
448 HEPES, pH 7.3 adjusted with NaOH), sandwiched between two copper carriers with a ring of
449 double-sided tape (140-µm thickness), and then frozen by a high pressure freezing machine.
450 The frozen samples were stored in liquid nitrogen until use.

451

452 **SDS-digested freeze-fracture replica labeling (SDS-FRL)**

453 The frozen samples were fractured into two parts at -130 °C and replicated by carbon (4-5 nm
454 thick), carbon-platinum (uni-direction from 60°, 2 nm), and carbon (20-25 nm) deposition in
455 a freeze-fracture machine (JFD-V, JOEL, Tokyo, Japan). The samples were digested with
456 2.5% SDS solution containing 0.1 M Tris-HCl (pH 8.3) at 80°C for 18-22 h. The replicas
457 were washed in the SDS solution and then a washing buffer (50 mM Tris-buffered saline

458 (TBS, pH 7.4) containing 0.1% BSA) at RT. To avoid non-specific binding of the probes and
459 antibodies, the replicas were blocked with 3% BSA, 2% cold fish skin gelatin, and 0.05%
460 Tween-20 in TBS for 1 h at RT. The replicas were incubated with 50 ng/ml GST-tagged PH
461 domain of phospholipase C δ1 (PI(4,5)P_2-Grip, Echelon Inc.) in a dilution buffer (1% BSA,
462 1% cold fish skin gelatin, and 0.05% Tween-20 in TBS) at 4°C overnight. Then the replica
463 was incubated with anti-GST antibody (rabbit IgG, 5 µg/ml, Bethyl Laboratories) and anti-
464 $Ca_V2.1$ antibody (guinea pig, 2.5 µg/ml, Synaptic Systems) as a marker of neurons at 15°C
465 overnight, and then gold-nanoparticle conjugated secondary antibodies (goat anti-rabbit IgG,
466 5 nm, 1:50, BBI; donkey anti-guinea pig IgG, 12 nm, 1:30, Jackson Immnoresearch)
467 dissolved in the dilution buffer at 15°C overnight. For double labeling of PI(4,5)P_2 with
468 proteins, the replicas were incubated with a mixture of primary antibodies (GluD2: rabbit
469 anti-GST IgG + guinea pig anti-GluD2 IgG (2.0 µg/ml, Frontier Institute); GIRK3: chicken
470 anti-GST IgY (5 µg/ml, Bethyl Laboratories) + rabbit anti-GIRK3 IgG (XX µg/ml, Frontier
471 Institute); mGluR1α: rabbit anti-GST IgG + guinea pig anti-mGluR1α IgG (XX µg/ml,
472 Frontier Institute)) at 15°C 1-2 overnight and then with gold-nanoparticle conjugated
473 secondary antibodies at 15°C overnight. After washing the replicas with the washing buffer,
474 they were picked up onto a grid coated with formvar in distilled water. Images were obtained
475 under TEM (Tecnai 10) with RADIUS software at magnifications of 65,000 and 39,000.

476

477 **Image analysis**

478 Images were analyzed with Darea software (Kleindienst et al., 2020), Fiji, and R. The gold
479 particle detection and the demarcation of the region of interest were performed on Darea
480 software. AZs on the P-face of PF boutons were indicated with the aggregation of
481 intramembrane particles on the replica at the electron microscopic level as described
482 previously (Eguchi et al., 2022, 2020; Harris and Landis, 1986; Landis and Reese, 1974;
483 Masugi-Tokita et al., 2007). Gold particles inside or < 30 nm away from the demarcation
484 border of AZs (outer rim) were counted as the particles in the AZs (Kleindienst et al., 2020).
485 Because the PSD area on the P-face of dendritic spines of PCs cannot be identified based on
486 morphological features, the largest cluster of GluD2-labeling gold particles on the spines was
487 identified as the PSD area (Eguchi et al., 2020; Luján et al., 2018a). The demarcated region
488 of the images was imported to R via FIJI/ImageJ for the following point pattern analysis.

Point pattern analysis of the gold particles described below was performed using spatstat package (version 2.3-0) of R (version 4.1.0). Nearest neighbor distances (NNDs) to both particles of the same size (e.g. from a 5 nm particle to the nearest 5 nm particle) and the other size (e.g. from a 5 nm particle to the nearest 10 nm particle) were computed to evaluate the distribution pattern of the particles. Center Periphery Index (CPI), indicating the location of the particles in the AZs or PSDs, was calculated as the square of the normalized distances from the center of the region of interest. When particles are randomly distributed in a circle, the mean CPI is near 0.5 (Kleindienst et al., 2020). To assess the randomness of the particle distribution, we performed two types of Monte-Carlo simulations, termed random and fitted simulations, following the methods described in the previous publications (Kleindienst et al., 2020; Luján et al., 2018b) using R. For the random simulation, particles were randomly placed on the demarcated area. The simulated particles were placed to keep the minimum distance of 10 nm from any other particles and then randomly shifted within a disc with a 30-nm diameter to reproduce the immunolabeling with a probe and antibodies (Tabata et al., 2019). In the fitted simulation, a constraint was added that the distance distribution between the simulated particles should not differ significantly from the distance distribution between the original particles. The particle distribution pattern was modeled and simulated as a Matern Cluster point process, and the goodness-of-fit between the real and simulated distribution was assessed by comparing both the all pairwise distances (APD) and NNDs of the particles using the two-sample *Kolmogorov-Smirnov* test (KS test), respectively, and considered them similar if the p-value was equal or above 0.1 for both. To avoid excessive statistical power due to the large sample size caused by a large number of particles, parametric bootstrapping was performed when the number of values to be compared exceeded 100. Specifically, we first randomly selected 100 distance values (NND or APD) from the simulated distribution and compared them to the empirical cumulative distribution function of the distance values of the real distribution using the KS test. This process was repeated 1,000 times, and the average of the p-values was used to assess the goodness-of-fit.

Gold particle clusters were detected with a hierarchical clustering algorithm called Ward linkage (Figure S1) and a density-based clustering algorithm called DBSCAN (Figures 2 and 3). For Ward linkage, the threshold distance was set as 50 nm. For DBSCAN, we set the minimum number of particles consisting of a cluster as 3 and the maximum distance between particles as the sum of the median and 1.5 times the interquartile range (IQR) of the NNDs. The area of the convex polygon connecting the outermost particles forming the cluster was

522 defined as the cluster area.

523

524 **Statistical analysis**

525 To consider the hierarchical structure, correlation, and probability distribution, data were
526 analyzed with either a linear mixed-effects model (LMM) or its generalized form (GLMM)
527 using the lme4 package (version 1.1-27.1) of R (Aarts et al., 2014; Yu et al., 2021).
528 Probability distributions for models were chosen by the goodness of fit to Poisson (for
529 discrete variables e.g. the number of particles), normal (e.g. CPI), or gamma distribution (for
530 continuous variables e.g. NNDs). Appropriate to the particular experiment and statistical
531 model, fixation methods (perfusion- and cryo-fixation), the faces of cell membranes (P- and
532 E-face), components of neurons (e.g. somata, spines, AZs on PF boutons), genotypes
533 (wildtype and Ts65Dn), and potentially their interactions were used as fixed effects, while
534 experiments, animals, replicas, and cells were used as random effects to consider the nested
535 and/or crossed data structure in the statistical analysis. For all experiments, at least four
536 animals per condition were used. All data are presented as estimated marginal means with
537 95% confidence intervals (CI, in figures) or standard error of means (s.e.m., in text) estimated
538 using the emmeans package. The goodness-of-fit of the models was assessed by second-order
539 Akaike Information Criterion (AICc) for the elimination of the random factors (MuMIn
540 package and then by likelihood ratio chi-square tests (Chi-LRT) with models in which the
541 fixed effects of interest had been dropped. For multiple pairwise comparisons between 3 or
542 more groups, posthoc comparisons to assume the significance of differences between pairs of
543 group means were performed using emmeans packages with Tukey (for all pairwise) or
544 Benjamini-Hochberg (BH, for selected pairwise) method when Chi-LRT detected a
545 significant difference ($p < 0.05$). Statistical significance was assumed if $p < 0.05$ (indicated
546 with blue or single asterisk), $p < 0.01$ (green or double asterisk), and $p < 0.001$ (red or triple
547 asterisk).

548

549 ## Author Contributions

550 KE and RS designed and conducted the experiments and wrote the manuscript. KE analyzed
551 the data.

Acknowledgment

We would like to thank Nicoleta Condruz (IST Austria, Klosterneuburg, Austria) for technical assistance with sample preparation; the Electron Microscopy Facility of IST Austria (Klosterneuburg, Austria) for technical support with EM works; Natalia Baranova (University of Vienna, Vienna, Austria) and Martin Loose (IST Austria, Klosterneuburg, Austria) for advice on liposome preparation; Yugo Fukazawa (University of Fukui, Fukui, Japan) for comments. This work was financially supported by funding from the Institute of Science and Technology Austria, the European Union's Horizon 2020 research and innovation program under the Marie Skłodowska-Curie grant agreement No. 793482 (to KE), and the European Research Council (ERC) grant agreement No. 694539 (to RS).

References

Aarts E, Verhage M, Veenvliet JV, Dolan CV, Van Der Sluis S. 2014. A solution to dependency: Using multilevel analysis to accommodate nested data. *Nature Neuroscience*. doi:10.1038/nn.3648

Aguado C, Colón J, Ciruela F, Schlaudraff F, Cabañero MJ, Perry C, Watanabe M, Liss B, Wickman K, Luján R. 2008. Cell type-specific subunit composition of G protein-gated potassium channels in the cerebellum. *J Neurochem* **105**:497–511.

Aktar S, Takatori S, Tsuji T, Orii M, Ohsaki Y, Cheng J, Fujimoto T. 2017. A New Electron Microscopic Method to Observe the Distribution of Phosphatidylinositol 3,4-bisphosphate. *Acta Histochem Cytochem* **50**:141–147.

Althof D, Baehrens D, Watanabe M, Suzuki N, Fakler B, Kulik Á. 2015. Inhibitory and excitatory axon terminals share a common nano-architecture of their Cav2.1 (P/Q-type) Ca(2+) channels. *Front Cell Neurosci* **9**:315.

Aoyagi K, Sugaya T, Umeda M, Yamamoto S, Terakawa S, Takahashi M. 2005. The activation of exocytotic sites by the formation of phosphatidylinositol 4,5-bisphosphate microdomains at syntaxin clusters. *J Biol Chem* **280**:17346–17352.

580 Borges-Merjane C, Kim O, Jonas P. 2020. Functional Electron Microscopy, “Flash and
581 Freeze,” of Identified Cortical Synapses in Acute Brain Slices. *Neuron* **105**:992–1006.e6.

582 Cheng J, Fujita A, Yamamoto H, Tatematsu T, Kakuta S, Obara K, Ohsumi Y, Fujimoto T.
583 2014. Yeast and mammalian autophagosomes exhibit distinct phosphatidylinositol 3-
584 phosphate asymmetries. *Nat Commun* **5**. doi:10.1038/ncomms4207

585 de Jong APH, Roggero CM, Ho MR, Wong MY, Brautigam CA, Rizo J, Kaeser PS. 2018.
586 RIM C2B Domains Target Presynaptic Active Zone Functions to PIP2-Containing
587 Membranes. *Neuron* **98**:335–349.e7.

588 Di Paolo G, De Camilli P. 2006. Phosphoinositides in cell regulation and membrane
589 dynamics. *Nature* **443**:651–657.

590 Eguchi K, Montanaro J, Le Monnier E, Shigemoto R. 2022. The Number and Distinct
591 Clustering Patterns of Voltage-Gated Calcium Channels in Nerve Terminals. *Front*
592 *Neuroanat* **16**. doi:10.3389/fnana.2022.846615

593 Eguchi K, Nakanishi S, Takagi H, Taoufiq Z, Takahashi T. 2012. Maturation of a PKG-
594 Dependent Retrograde Mechanism for Exoendocytic Coupling of Synaptic Vesicles. *Neuron*
595 **74**:517–529.

596 Eguchi K, Velicky P, Hollergschwandtner E, Itakura M, Fukazawa Y, Danzl JG, Shigemoto
597 R. 2020. Advantages of Acute Brain Slices Prepared at Physiological Temperature in the
598 Characterization of Synaptic Functions. *Front Cell Neurosci* **14**:63.

599 Falkenburger BH, Jensen JB, Dickson EJ, Suh BC, Hille B. 2010. Phosphoinositides: Lipid
600 regulators of membrane proteins. *J Physiol* **588**:3179–3185.

601 Fernández-Alacid L, Aguado C, Ciruela F, Martín R, Colón J, Cabañero MJ, Gassmann M,
602 Watanabe M, Shigemoto R, Wickman K, Bettler B, Sánchez-Prieto J, Luján R. 2009.
603 Subcellular compartment-specific molecular diversity of pre- and post-synaptic GABA-
604 activated GIRK channels in Purkinje cells: Pre- and post-synaptic GABAB-activated GIRK
605 channels in PCs. *J Neurochem* **110**:1363–1376.

606 Fujita A, Cheng J, Tauchi-Sato K, Takenawa T, Fujimoto T. 2009. A distinct pool of
607 phosphatidylinositol 4,5-bisphosphate in caveolae revealed by a nanoscale labeling
608 technique. *Proc Natl Acad Sci U S A* **106**:9256–9261.

609 Harris KM, Landis DM. 1986. Membrane structure at synaptic junctions in area CA1 of the
610 rat hippocampus. *Neuroscience* **19**:857–872.

611 Haucke V. 2005. Phosphoinositide regulation of clathrin-mediated endocytosis. *Biochem Soc*
612 *Trans* **33**:1285–1289.

613 Honigmann A, van den Bogaart G, Iraheta E, Risselada HJ, Milovanovic D, Mueller V,
614 Müllar S, Diederichsen U, Fasshauer D, Grubmüller H, Hell SW, Eggeling C, Kühnel K,
615 Jahn R. 2013. Phosphatidylinositol 4,5-bisphosphate clusters act as molecular beacons for
616 vesicle recruitment. *Nat Struct Mol Biol* **20**:679–686.

617 Idevall-Hagren O, De Camilli P. 2015. Detection and manipulation of phosphoinositides.
618 *Biochim Biophys Acta* **1851**:736–745.

619 Kleindienst D, Montanaro J, Bhandari P, Case MJ, Fukazawa Y, Shigemoto R. 2020. Deep
620 Learning-Assisted High-Throughput Analysis of Freeze-Fracture Replica Images Applied to
621 Glutamate Receptors and Calcium Channels at Hippocampal Synapses. *Int J Mol Sci* **21**.
622 doi:10.3390/ijms21186737

623 Landis DM, Reese TS. 1974. Differences in membrane structure between excitatory and
624 inhibitory synapses in the cerebellar cortex. *J Comp Neurol* **155**:93–125.

625 Lei W, Myers KR, Rui Y, Hladyshau S, Tsygankov D, Zheng JQ. 2017. Phosphoinositide-
626 dependent enrichment of actin monomers in dendritic spines regulates synapse development
627 and plasticity. *J Cell Biol* **216**:2551–2564.

628 Luján R, Aguado C, Ciruela F, Arus XM, Martín-Belmonte A, Alfaro-Ruiz R, Martínez-
629 Gómez J, de la Ossa L, Watanabe M, Adelman JP, Shigemoto R, Fukazawa Y. 2018a. SK2
630 Channels Associate With mGlu1α Receptors and CaV2.1 Channels in Purkinje Cells. *Front*
631 *Cell Neurosci* **12**:311.

632 Luján R, Aguado C, Ciruela F, Cózar J, Kleindienst D, de la Ossa L, Bettler B, Wickman K,
633 Watanabe M, Shigemoto R, Fukazawa Y. 2018b. Differential association of GABAB
634 receptors with their effector ion channels in Purkinje cells. *Brain Struct Funct* **223**:1565–
635 1587.

636 Maekawa M, Fairn GD. 2014. Molecular probes to visualize the location, organization and
637 dynamics of lipids. *J Cell Sci* **127**:4801–4812.

638 Martin TFJ. 2001. PI(4,5) P2 regulation of surface membrane traffic. *Curr Opin Cell Biol*
639 **13**:493–499.

640 Masugi-Tokita M, Tarusawa E, Watanabe M, Molnar E, Fujimoto K, Shigemoto R. 2007.
641 Number and Density of AMPA Receptors in Individual Synapses in the Rat Cerebellum as
642 Revealed by SDS-Digested Freeze-Fracture Replica Labeling. *Journal of Neuroscience*
643 **27**:2135–2144.

644 Milovanovic D, Platen M, Junius M, Diederichsen U, Schaap IAT, Honigmann A, Jahn R,
645 Van Den Bogaart G. 2016. Calcium promotes the formation of syntaxin 1 mesoscale domains
646 through phosphatidylinositol 4,5-bisphosphate. *J Biol Chem* **291**:7868–7876.

647 Ozato-Sakurai N, Fujita A, Fujimoto T. 2011. The distribution of phosphatidylinositol 4,5-
648 bisphosphate in acinar cells of rat pancreas revealed with the Freeze-Fracture replica labeling
649 method. *PLoS One* **6**. doi:10.1371/journal.pone.0023567

650 Petersen EN, Chung H-W, Nayebosadri A, Hansen SB. 2016. Kinetic disruption of lipid rafts
651 is a mechanosensor for phospholipase D. *Nat Commun* **7**:13873.

652 Posor Y, Eichhorn-Grünig M, Haucke V. 2015. Phosphoinositides in endocytosis. *Biochimica*
653 *et Biophysica Acta - Molecular and Cell Biology of Lipids* **1851**:794–804.

654 Suh B-C, Hille B. 2008. PIP2 is a necessary cofactor for ion channel function: how and why?
655 *Annu Rev Biophys* **37**:175–195.

656 Suh B-C, Kim D-I, Falkenburger BH, Hille B. 2012. Membrane-localized -subunits alter the
657 PIP2 regulation of high-voltage activated Ca2+ channels. *Proceedings of the National*
658 *Academy of Sciences* **109**:3161–3166.

659 Szoboszlay M, Kirizs T, Nusser Z. 2017. Objective quantification of nanoscale protein
660 distributions. *Sci Rep* **7**:15240.

661 Tabata S, Jevtic M, Kurashige N, Fuchida H, Kido M, Tani K, Zenmyo N, Uchinomiya S,
662 Harada H, Itakura M, Hamachi I, Shigemoto R, Ojida A. 2019. Electron Microscopic
663 Detection of Single Membrane Proteins by a Specific Chemical Labeling. *iScience* **22**:256–
664 268.

665 Tanaka KAK, Suzuki KGN, Shirai YM, Shibutani ST, Miyahara MSH, Tsuboi H, Yahara M,
666 Yoshimura A, Mayor S, Fujiwara TK, Kusumi A. 2010. Membrane molecules mobile even

667 after chemical fixation. *Nat Methods* **7**:865–866.

668 Taoufiq Z, Eguchi K, Takahashi T. 2013. Rho-Kinase Accelerates Synaptic Vesicle
669 Endocytosis by Linking Cyclic GMP-Dependent Protein Kinase Activity to
670 Phosphatidylinositol-4,5-Bisphosphate Synthesis. *Journal of Neuroscience* **33**:12099–12104.

671 Tsuji T, Takatori S, Fujimoto T. 2019. Definition of phosphoinositide distribution in the
672 nanoscale. *Current Opinion in Cell Biology*. doi:10.1016/j.ceb.2018.10.008

673 Ueda Y, Hayashi Y. 2013. PIP3 Regulates Spinule Formation in Dendritic Spines during
674 Structural Long-Term Potentiation. *Journal of Neuroscience* **33**:11040–11047.

675 van den Bogaart G, Meyenberg K, Risselada HJ, Amin H, Willig KI, Hubrich BE, Dier M,
676 Hell SW, Grubmüller H, Diederichsen U, Jahn R. 2011. Membrane protein sequestering by
677 ionic protein-lipid interactions. *Nature* **479**:552–555.

678 Wang J, Richards DA. 2012. Segregation of PIP2 and PIP3 into distinct nanoscale regions
679 within the plasma membrane. *Biol Open* **1**:857–862.

680 Wenk MR, De Camilli P. 2004. Protein-lipid interactions and phosphoinositide metabolism in
681 membrane traffic: Insights from vesicle recycling in nerve terminals. *Proceedings of the*
682 *National Academy of Sciences* **101**:8262–8269.

683 Whorton MR, MacKinnon R. 2011. Crystal structure of the mammalian GIRK2 K+ channel
684 and gating regulation by G proteins, PIP2, and sodium. *Cell* **147**:199–208.

685 Yu Z, Guindani M, Grieco SF, Chen L, Holmes TC, Xu X. 2021. Beyond t test and ANOVA:
686 applications of mixed-effects models for more rigorous statistical analysis in neuroscience
687 research. *Neuron*. doi:10.1016/j.neuron.2021.10.030

688

689

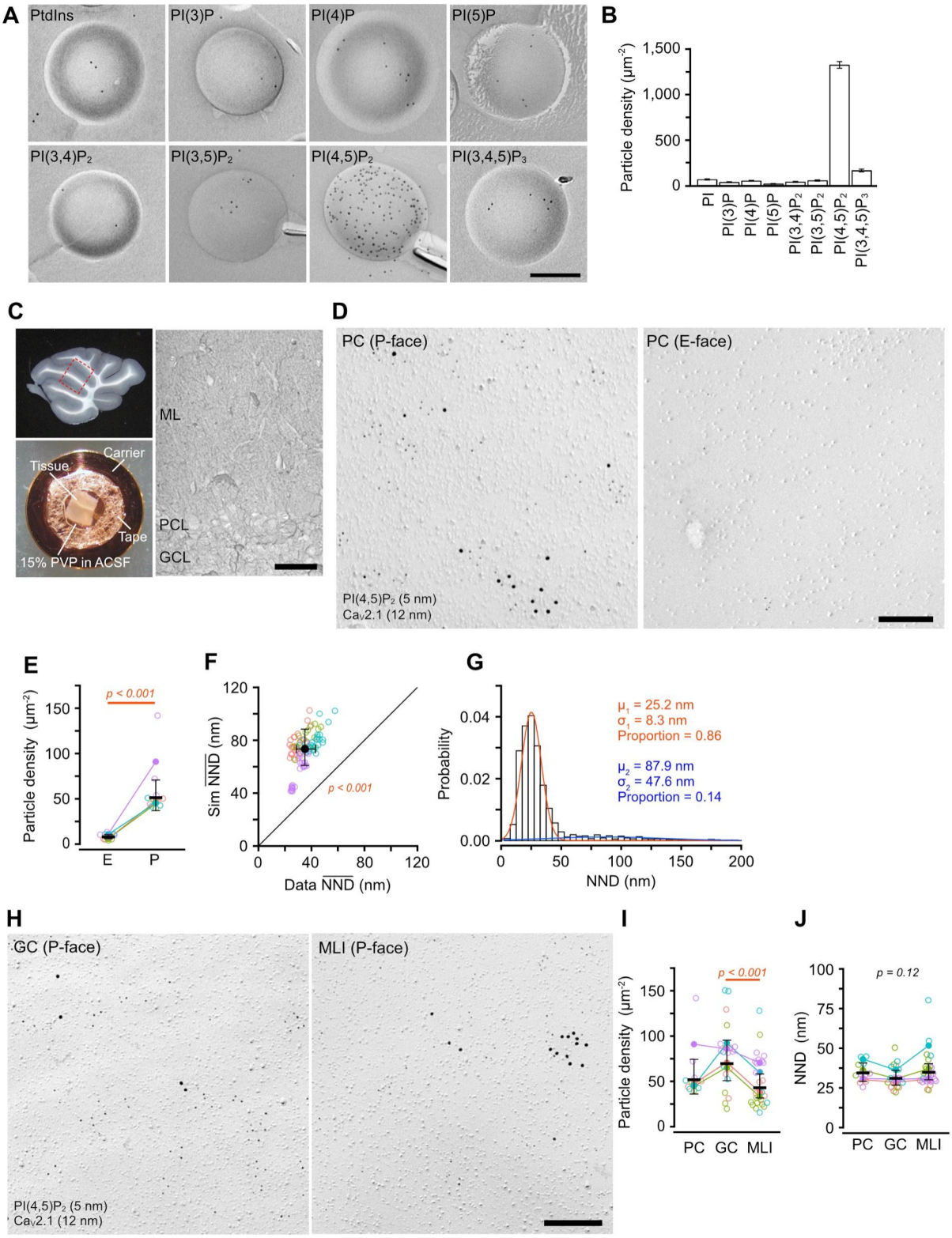

Figure 1. SDS-FRL of PI(4,5)P_2 on somatic membranes of mouse cerebellar neurons.

(**A-B**) Specificity of PI(4,5)P_2 labeling. Replicas of liposomes containing 5% PtdIns or different stereoisomers of PIs were labeled using GST-PH, anti-GST antibody, and 5-nm gold

694 particle-conjugated secondary antibody (**A**, Scale bar = 200 nm). The density of gold
695 particles was highest in the liposome containing PI(4,5)P_2 (**B**).

696 (**C**) Acute cerebellar slice preparation for high-pressure freezing (HPF) and replica
697 preparation. Left-top, an acute sagittal slice of the mouse cerebellum. The dashed line
698 indicates the trimmed region for HPF. Left-bottom, a trimmed cerebellar slice on a copper
699 carrier with double-sided tape for HPF. Right, low-magnification transmission electron
700 microscopic (TEM) image of the mouse cerebellar replica containing granule cell layer
701 (GCL), Purkinje cell layer (PCL), and molecular layer (ML). Scale bar = 20 µm.

702 (**D**) Example TEM image of 5-nm gold particle labeling for PI(4,5)P_2 with immunogold
703 labeling for $Ca_V2.1$ (12 nm) on P- (left) and E-face (right) of the PC somatic membranes of
704 cerebellar PC. Scale bar = 200 nm.

705 (**E**) Statistical comparison of the PI(4,5)P_2 particle density on the E-face and P-face of the PC
706 somatic membranes. Open and closed circles indicate the means of the PI(4,5)P_2 particle
707 density in each PC and each mouse, respectively, with different colors. Black horizontal bars
708 indicate estimated marginal means (emmeans, thick bars) and 95% confidence intervals (CIs,
709 error bars) of the density estimated by GLMM (Methods). The PI(4,5)P_2 density was
710 significantly higher on the P-face than on the E-face of the PC somatic membranes (P-face:
711 51.2 ± 8.5 particles/μm^2, E-face: 8.0 ± 1.2 particles/μm^2, n = 213 images/12 cells/4 mice, $p <$
712 0.001, Chi-square likelihood ratio test (Chi-LRT)).

713 (**F**) Comparison of nearest neighbor distances (NND) between real (Data NND, x-axis) and
714 simulated (Sim NND, y-axis) PI(4,5)P_2 particles on PC somatic membranes. Data-NNDs are
715 significantly smaller than Sim NNDs (Data: 35.1 ± 3.6 nm, Sim: 73.3 ± 7.0 nm, n = 206
716 images/11 cells/4 mice, $p < 0.001$, Chi-LRT).

717 (**G**) Distribution of NNDs of the PI(4,5)P_2 particles obtained from a single PC somatic
718 membrane (n = 2,929 particles). Red and blue lines indicate the distinct components of the
719 NND distribution estimated from the Gaussian mixture modeling.

720 (**H**) PI(4,5)P_2 labeling (5 nm) with $Ca_V2.1$ (12 nm) on the P-face of GC (left) and molecular
721 layer interneuron (MLI, right) somatic membranes. Scale bar = 200 nm.

722 (**I**) The PI(4,5)P_2 particle density on the somatic membranes (P-face) of different neuronal
723 cell types in the mouse cerebellum (PC: 51.8 ± 9.6 particles/μm^2, GC: 69.8 ± 11.3

724 particles/μm^2, MLI: 42.9 ± 6.7 particles/μm^2, n = 273 images/57 cells/4 mice, p = 0.003, Chi-
725 LRT).

726 (**J**) NND of the $PI(4,5)P_2$ particles on the somatic membranes of different neuronal cell types
727 in the mouse cerebellum (PC: 34.4 ± 3.0 nm, GC: 31.0 ± 2.4 nm, MLI: 34.8 ± 2.6 nm, n =
728 65,607 values/57 cells/4 mice, p = 0.12, Chi-LRT).

729

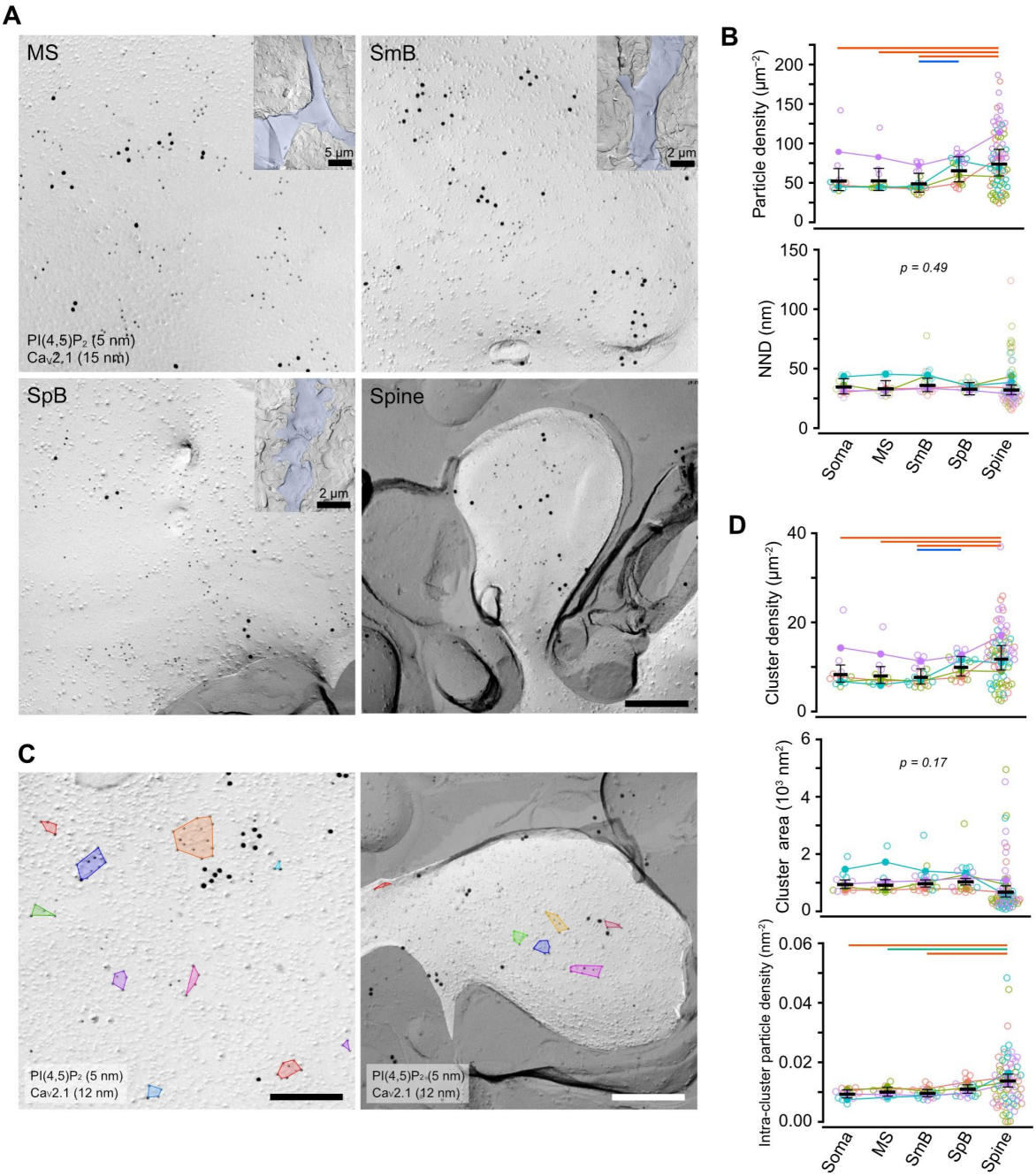

Figure 2. PI(4,5)P_2 particle distribution on somatodendritic membranes of PCs.

(**A**) Example images obtained from the different compartments of PC dendritic membranes: main shaft (MS, top-left), smooth branchlet (SmB, top-right), spiny branchlet (SpB, bottom-left), and spine (bottom-right). Scale bar = 200 nm. Inset: low-magnification images of MS, SmB, and SpB, respectively, indicated with blue.

(**B**) Comparison of the PI(4,5)P_2 particle density (top) and NNDs (bottom) in the somatodendritic membrane compartments of PCs. The PI(4,5)P_2 density gradually increased

738 from soma and proximal dendrites to distal dendritic components (top, n = 611 images/134
739 components/4 mice, $p < 0.001$, Chi-LRT), whereas no significant difference in NNDs was
740 detected between these compartments (bottom, n = 67,380 values/134 components/4 mice, p
741 = 0.49, Chi-LRT).

742 (**C**) Example images of the $PI(4,5)P_2$ clusters on the somatic (left) and spine (right)
743 membrane of PCs. Colored polygons indicate individual $PI(4,5)P_2$ clusters detected by the
744 DBSCAN algorithm. Scale bars = 200 nm.

745 (**D**) Quantitative analysis of the $PI(4,5)P_2$ clusters on the somatodendritic compartments of
746 PCs. Top, the number of clusters per area (cluster density, n = 611 values/134 components/4
747 mice). Middle, the cluster area (10,479 clusters/124 components/4 mice). Bottom, the intra-
748 cluster particle density (10,343 clusters/134 components/4 mice). The cluster density and the
749 intra-cluster particle density are significantly higher in spine membranes compared to the
750 somatic and proximal dendritic membranes ($p < 0.001$, Chi-LRT), whereas there is no
751 significant difference in the cluster area ($p = 0.17$, Chi-LRT).

752

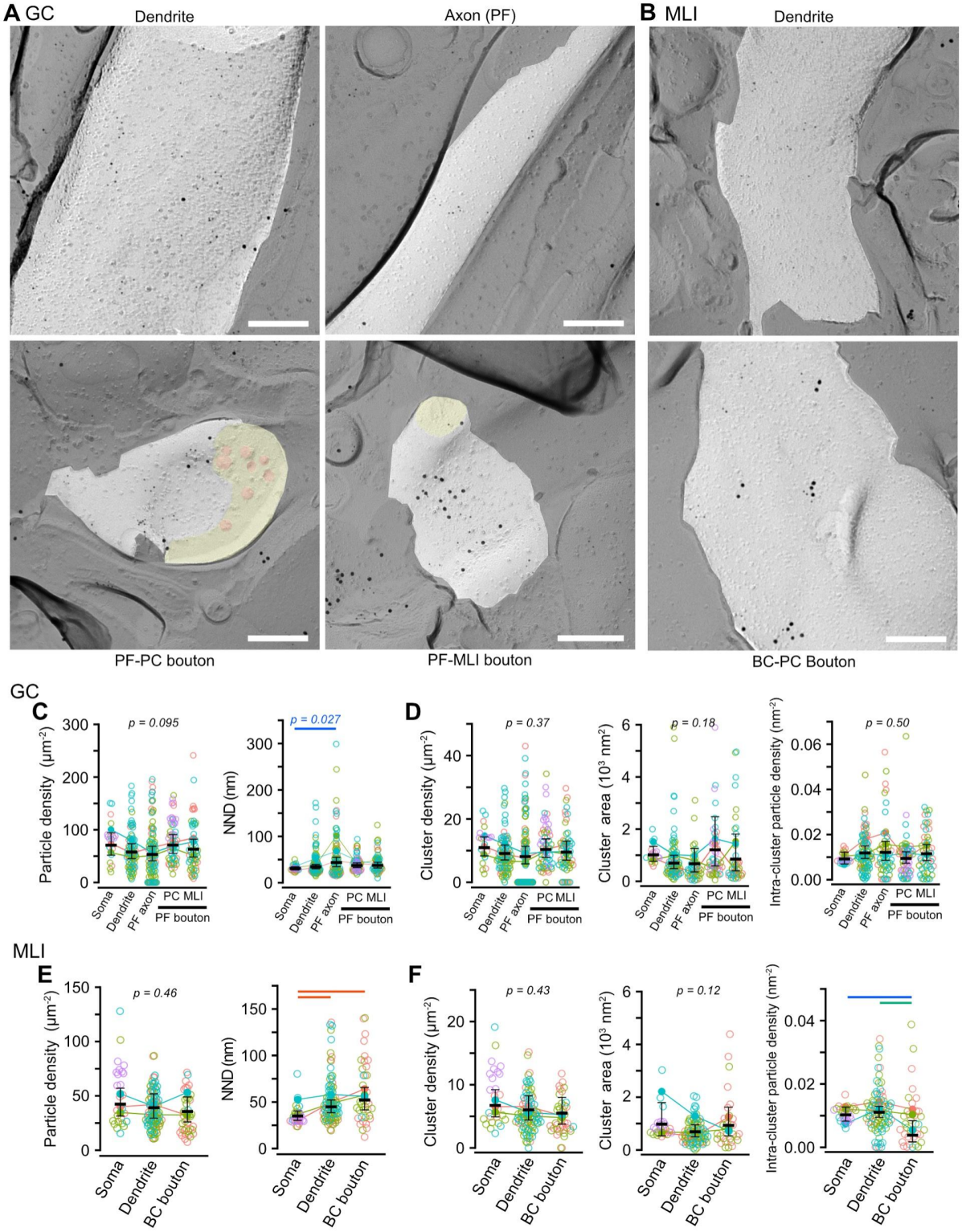

Figure 3. PI(4,5)P_2 particle distribution in GCs and MLIs.

(**A**) Example images obtained from the different compartments of GC membranes: dendrites (top-left), parallel fiber (PF) axons (top-right), presynaptic PF boutons on the PC spine (PC-PF, bottom-left) and on the MLI dendrite (PF-MLI, bottom-right). Yellow and orange in the

758 PF boutons indicate the cross-fracture and synaptic vesicle membranes, respectively. Scale
759 bars = 200 nm.

760 (**B**) Example images obtained from different compartments of MLI membranes: dendrites
761 (top) and basket cell (BC) presynaptic bouton on PC soma (bottom). Scale bar = 200 nm.

762 (**C**) Comparison of the PI(4,5)P_2 particle density (left) and NNDs (right) in the different GC
763 membrane compartments. NNDs show significant differences between the compartments (n =
764 67,380 values/134 components/4 mice, $p < 0.001$, Chi-LRT), whereas there is no significance
765 in the density (n = 376 images/320 components/4 mice, p = 0.09, Chi-LRT).

766 (**D**) Quantitative analysis of the PI(4,5)P_2 particle clusters in different GC membrane
767 compartments. There are no significant differences in the cluster density (n = 376 images/320
768 components/4 mice, p = 0.37, Chi-LRT), the cluster area (n = 4070 clusters/254
769 components/4 mice, p = 0.18, Chi-LRT), and the intra-cluster particle density (n = 4004
770 clusters/253 compartments/4 mice, p = 0.50, Chi-LRT).

771 (**E**) Comparison of the PI(4,5)P_2 particle density (left) and NNDs (right) in different
772 membrane compartments of MLIs. NNDs in dendritic and BC bouton membranes are
773 significantly larger than that in somatic membranes (n = 24,012 values/152 components/4
774 mice, $p < 0.001$, Chi-LRT), whereas there is no significant difference in the density between
775 the compartments (n = 230 images/153 components/4 mice, p = 0.46, Chi-LRT).

776 (**F**) Quantitative analysis of the PI(4,5)P_2 particle clusters in different MLI membrane
777 compartments. The intra-cluster particle density in BC bouton membranes is significantly
778 smaller than the other components (n = 3,766 clusters/149 components/4 mice, p = 0.03, Chi-
779 LRT), whereas no significant difference was detected in the cluster density (n = 230
780 images/153 components/4 mice, p = 0.43, Chi-LRT) and the cluster area (n = 3,822
781 clusters/146 components/4 mice, p = 0.12, Chi-LRT) between these compartments.

782

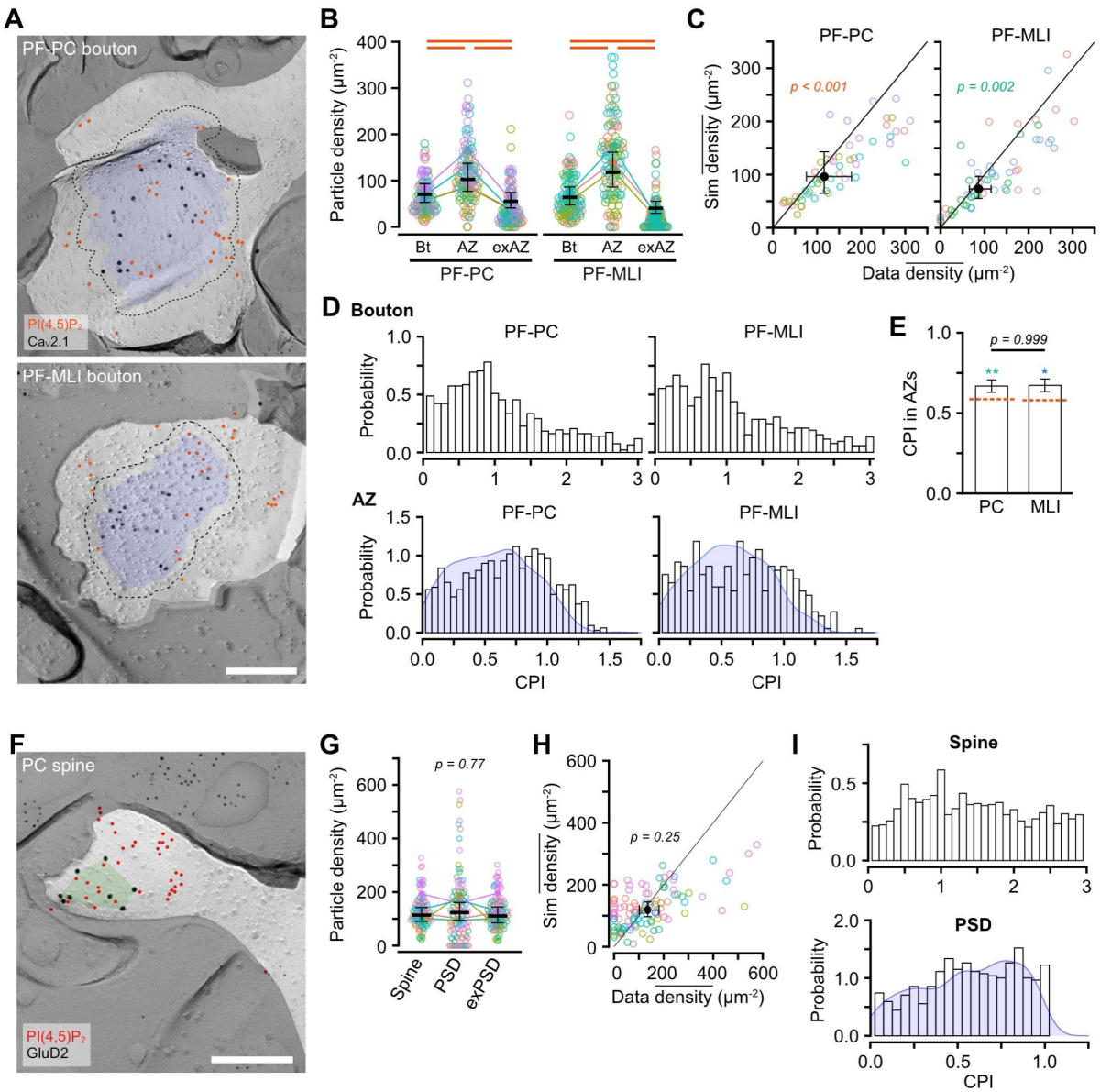

Figure 4. PI(4,5)P_2 distribution in pre- and post-synaptic membranes of PF-PC synapses.

(**A**) Example images for PI(4,5)P_2 particle distribution on the membranes of PF-PC (top) and PF-MLI bouton (bottom). Red and black circles indicate gold particles for PI(4,5)P_2 and $Ca_V2.1$, respectively. The Blue area and dotted line indicate AZ and outer-rim (30 nm from the edge of AZ, Methods), respectively. Scale bar = 200 nm.

(**B**) Beeswarm plot of the PI(4,5)P_2 density in the whole bouton (Bt), AZs, and extra-AZ region (exAZ) of the PF-PC (left) and PF-MLI (right) bouton membranes. The PI(4,5)P_2 density was significantly higher in AZs than in the whole bouton and the exAZ in both PF-PC and PF-MLI boutons (n = 111 boutons/4 mice, $p < 0.001$, Tukey method).

794 (**C**) Comparison of the $PI(4,5)P_2$ density in the AZs between real and simulated random
795 distribution on the PF bouton membranes. The density of the real particle distribution was
796 significantly higher than that of the simulated one in both PF-PC (real: 97.2 ± 19.7
797 particles/μm^2, sim: 66.7 ± 13.5 particles/μm^2, n = 55 boutons/4 mice, $p < 0.001$, Chi-LRT)
798 and PF-MLI (real 86.7 ± 12.4 particles/μm^2, sim: 73.2 ± 10.4 particles/μm^2, n = 56 boutons/4
799 mice, p = 0.002, Chi-LRT) AZ membranes.

800 (**D**) Distribution of center-periphery index (CPI) of $PI(4,5)P_2$ particles in boutons (top) and
801 AZs (bottom). Blue in the bottom graph indicates the CPI distribution of the simulated
802 particles that are randomly distributed in AZs.

803 (**E**) Comparison of CPIs of the $PI(4,5)P_2$ particles in AZs between PF-PC and PF-MLI AZs.
804 There is no significant difference in the CPIs between PF-PC and PF-MLI AZs (PF-PC: 0.67
805 ± 0.02, PF-MLI: 0.67 ± 0.02, n = 107 boutons/4 mice, p = 0.999, Chi-LRT). Dashed lines
806 with red show the mean CPIs of the simulated randomly-distributed particles. Asterisks on
807 the bars indicate statistical differences in CPIs between real and simulated particles (PF-PC:
808 0.59 ± 0.02, PF-MLI: 0.58 ± 0.02, *$p < 0.05$, **$p < 0.01$, Tukey method).

809 (**F**) Example images of the $PI(4,5)P_2$ particle distribution on the PC spine membrane. Red and
810 black circles indicate $PI(4,5)P_2$ and GluD2, respectively. The green area indicates
811 postsynaptic density (PSD) based on the cluster of GluD2. Scale bar = 200 nm.

812 (**G**) Beeswarm plot of the $PI(4,5)P_2$ density in the whole spine (spine), PSD, and extra-PSD
813 region (exPSD) of the PC spine membranes. No significant difference in the density was
814 detected between these compartments (n = 108 spines/6 mice, p = 0.77, Chi-LRT).

815 (**H**) Comparison of the $PI(4,5)P_2$ density in the PSDs between real and simulated random
816 distribution on the PC spine membranes. The density of the real and simulated particle
817 distribution was not significantly different (real: 0.59 ± 0.01, sim: 0.55 ± 0.01, n = 108
818 spines/6 mice, p = 0.25, Chi-LRT).

819 (**I**) Distribution of CPIs of $PI(4,5)P_2$ particles in spines (top) and PSDs (bottom). Blue in the
820 bottom graph indicates the CPI distribution of the simulated particles that are randomly
821 distributed in PSDs. The CPI of the $PI(4,5)P_2$ particles is uniformly distributed in the spines
822 and PSDs, suggesting the random distribution of $PI(4,5)P_2$.

823

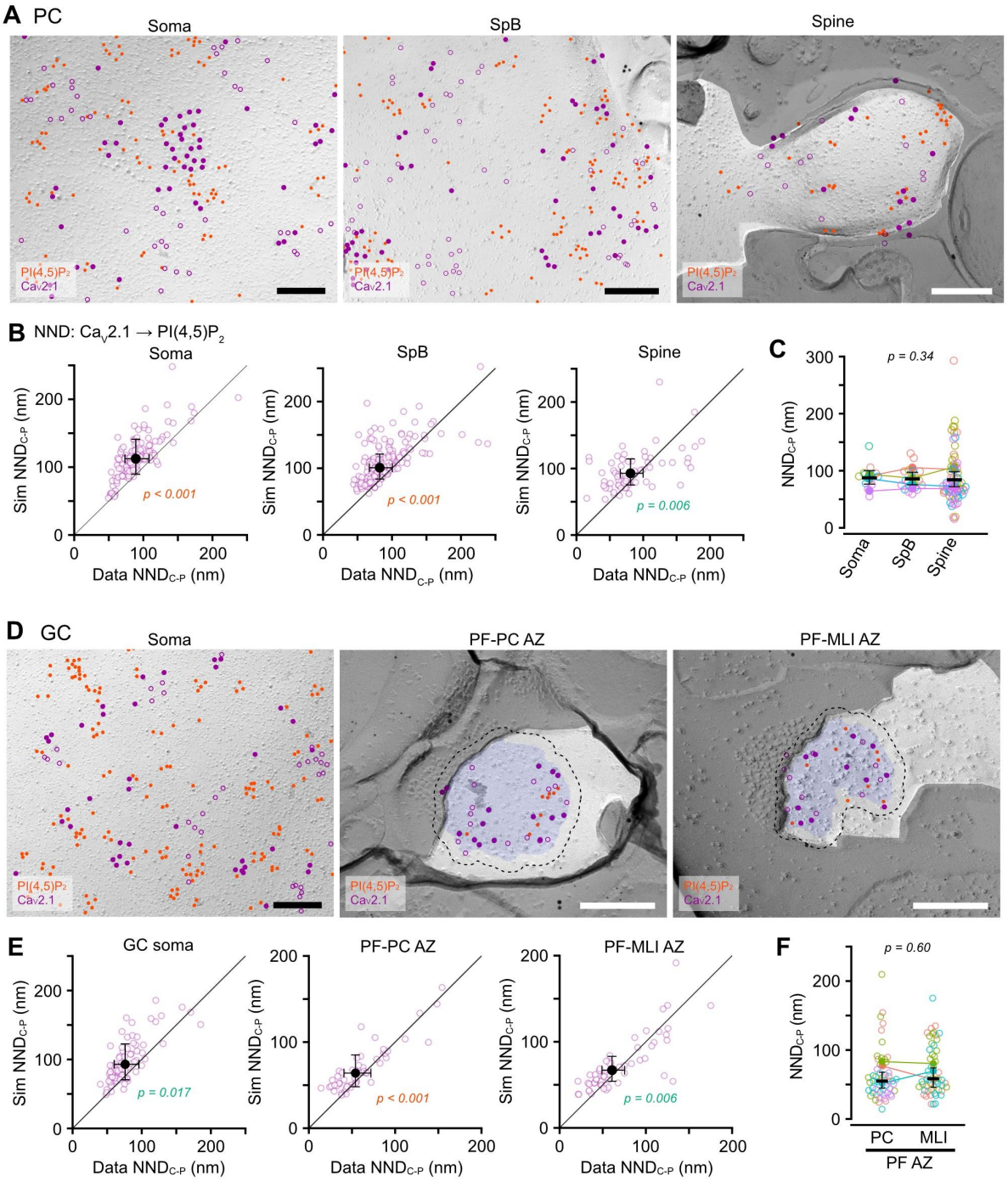

Figure 5. Ubiquitous association of $Ca_V2.1$ with $PI(4,5)P_2$ on cell membranes of PCs and GCs.

(**A**) Example images for co-immunolabeling of $PI(4,5)P_2$ and $Ca_V2.1$ on somatic (left), SpB (middle), and spine (right) membranes of the PC. Red and purple (closed, open) circles indicate $PI(4,5)P_2$ and $Ca_V2.1$ (real, fitted-simulated) particles, respectively. Scale bars = 200 nm.

(**B**) Comparison of the NNDs from $Ca_V2.1$ to $PI(4,5)P_2$ particles (NND_{C-P}) between real and fitted-simulated $Ca_V2.1$ distribution on somatic (left), SpB (middle), and spine (right) membranes of PCs. The NND_{C-P} of the real distribution was significantly smaller than that of the simulated one in somatic (real: 89.7 ± 9.6 nm, sim: 112.9 ± 12.1 nm, n = 129 images/14 cells/5 mice, $p < 0.001$, Chi-LRT), SpB (real: 82.3 ± 8.1 nm, sim: 100.5 ± 9.9 nm, n = 158 images/20 dendrites/4 mice, $p < 0.001$, Chi-LRT), and spine membrane (real: 80.9 ± 8.7 nm, sim: 92.8 ± 9.9 nm, 69 spines/4 mice, p = 0.006, Chi-LRT).

(**C**) Comparison of NND_{C-P} between somatodendritic compartments. There is no significant difference between the PC compartments (n = 12,956 values/92 components/5 mice, p = 0.70, Chi-LRT).

(**D**) Example images for co-immunolabeling of $PI(4,5)P_2$ and $Ca_V2.1$ on somatic (left) and presynaptic PF-PC (middle) and PF-MLI (right) AZ membranes of the GC. Red and purple (closed, open) circles indicate $PI(4,5)P_2$ and $Ca_V2.1$ (real, fitted-simulated) particles, respectively. The Blue area and dotted lines indicate AZs and the outer-rim, respectively. Scale bars = 200 nm.

(**E**) Comparison of the NND_{C-P} between real and fitted-simulated $Ca_V2.1$ distribution on somatic (left), PF-PC AZ (middle), and PF-MLI AZ (right) membranes of GCs.The NND_{C-P} of the real distribution was significantly smaller than that of the simulated one in somatic (real: 76.0 ± 9.0 nm, sim: 93.0 ± 13.1 nm, n = 81 images/25 cells/5 mice, p = 0.017, Chi-LRT), PF-PC AZ (real: 54.0 ± 7.9 nm, sim: 64.0 ± 9.3 nm, n = 54 AZs/4 mice, $p < 0.001$, Chi-LRT), and PF-MLI AZ membrane (real: 60.8 ± 6.7 nm, sim: 67.0 ± 7.3 nm, 52 AZs/4 mice, p = 0.006, Chi-LRT).

(**F**) Comparison of NND_{C-P} between presynaptic AZs of PF-PC and PF-MLI synapses. There is no significant difference in NND_{C-P} between the AZs (n = 1,110 values/68 AZs/4 mice, p = 0.60, Chi-LRT).

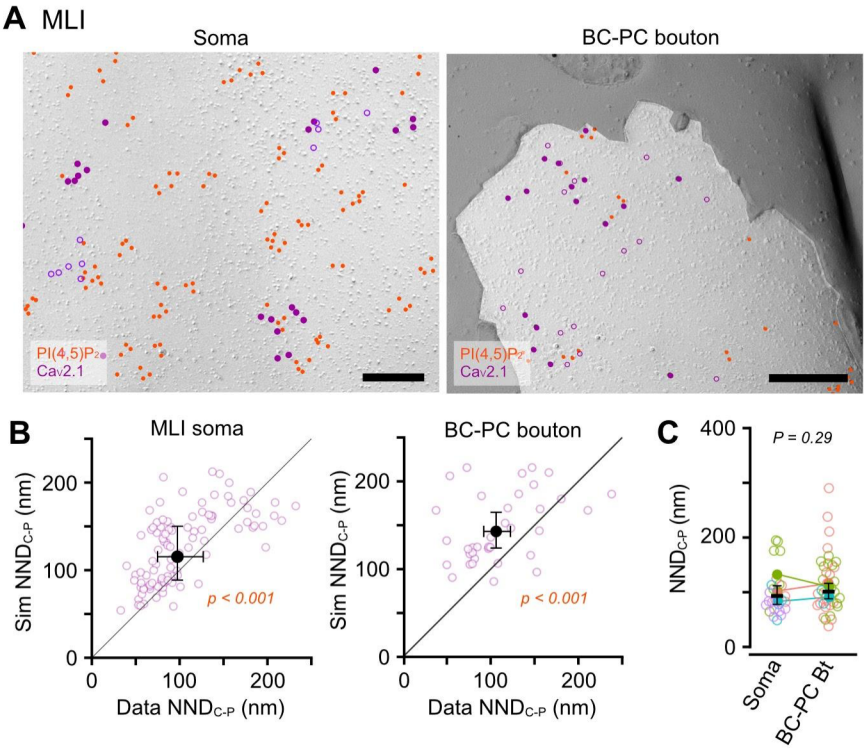

857

858 **Figure 6. Association of $Ca_V2.1$ with $PI(4,5)P_2$ on cell membranes of MLIs.**

859 (**A**) Example images for co-immunolabeling of $PI(4,5)P_2$ and $Ca_V2.1$ on somatic (left) and
860 basket cell (BC)-PC bouton (right) membranes of the MLI. Red and purple (closed, open)
861 circles indicate $PI(4,5)P_2$ and $Ca_V2.1$ (real, fitted-simulated) particles, respectively. P-face of
862 BC-PC boutons were identified based on $Ca_V2.1$ clusters and the surrounding E-face of the
863 PC somatic membranes with $Ca_V2.1$ clusters. Scale bars = 200 nm.

864 (**B**) Comparison of the NND_{C-P} between real and fitted-simulated $Ca_V2.1$ distribution on
865 somatic (left) and BC-PC bouton (right) membranes of MLIs. The NND_{C-P} of the real
866 distribution was significantly smaller than that of the simulated one in somatic (real: 97.5 ±
867 13.1 nm, sim: 115.4 ± 15.5 nm, n = 102 images/26 cells/4 mice, $p < 0.001$, Chi-LRT) and
868 BC-PC bouton membrane (real: 106.0 ± 7.7 nm, sim: 143.0 ± 10.4 nm, 37 boutons/3 mice, p
869 = 0.006, Chi-LRT).

870 (**C**) Comparison of NND_{C-P} between somatic and bouton membranes. No significant
871 difference was shown between these compartments (n = 2,854 values/63 components/4 mice,
872 p = 0.29, Chi-LRT).

873

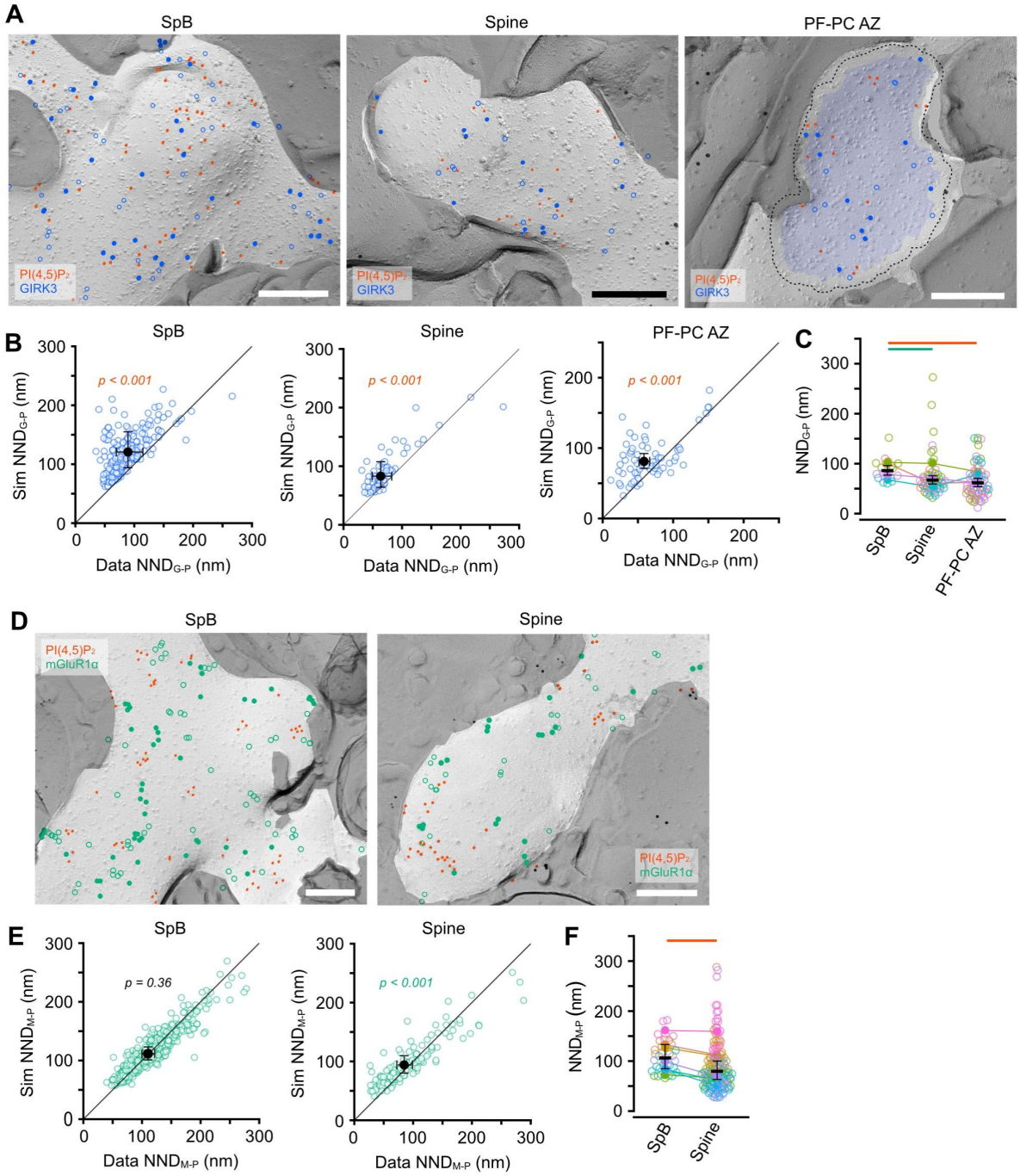

Figure 7. Association of GIRK3 channels and mGluR1α receptors with PI(4,5)P_2 on cell membranes of cerebellar neurons.

(**A**) Example images for co-labeling of PI(4,5)P_2 and GIRK3 channels on PC SpB (left), PC spine (middle), and PF-PC AZ (right) membranes. Red and blue (closed, open) circles indicate PI(4,5)P_2 and GIRK3 (real, fitted-simulated) particles, respectively. The Blue area and a dotted line on the left indicate the AZ and the outer-rim, respectively. Scale bars = 200 nm.

882 (**B**) Comparison of the NNDs from GIRK3 to PI(4,5)P_2 particles (NND_{G-P}) between real and
883 fitted-simulated GIRK3 distribution on PC SpB (left), PC spine (middle), and PF-PC AZ
884 (right) membranes. The NND_{G-P} of the real distribution was significantly smaller than that of
885 the simulated one in SpB (real: 89.3 ± 11.4 nm, sim: 120.7 ± 15.4 nm, n = 88 images/19
886 dendrites/5 mice, $p < 0.001$, Chi-LRT), spine (real: 63.6 ± 8.4 nm, sim: 83.0 ± 11.0 nm, n =
887 57 spines/4 mice, $p < 0.001$, Chi-LRT), and PF-PC AZ membrane (real: 58.6 ± 3.9 nm, sim:
888 81.1 ± 5.3 nm, 65 AZs/4 mice, $p < 0.001$, Chi-LRT).

889 (**C**) Comparison of NND_{G-P} between the post- and presynaptic compartments of cerebellar
890 neurons. The NND_{G-P} was significantly shorter in the spine and AZ membranes than in the
891 SpB membrane (4,730 values/90 compartments/4 mice, $p < 0.001$, Chi-LRT).

892 (**D**) Example images for co-labeling of PI(4,5)P_2 and mGluR1α receptors on PC SpB (left)
893 and spine (right) membranes. Red and green (closed, open) circles indicate PI(4,5)P_2 and
894 mGluR1α (real, fitted-simulated) particles, respectively. Scale bars = 200 nm.

895 (**E**) Comparison of the NNDs from mGluR1α to PI(4,5)P_2 particles (NND_{M-P}) between real
896 and fitted-simulated mGluR1α distribution on PC SpB (left) and spine (right) membranes.
897 The NND_{M-P} of the real distribution was significantly smaller than that of the simulated one
898 in the spine membranes (real: 81.8 ± 18.4 nm, sim: 91.2 ± 20.6 nm, n = 140 spines/7 mice, p
899 < 0.001, Chi-LRT), but not in the SpB membrane (n = 147 images/35 dendrites/7 mice, p =
900 0.36, Chi-LRT).

901 (**F**) Comparison of NND_{M-P} between the SpB and spine membranes of PCs. The NND_{M-P} was
902 shorter in the spines than in the SpB membrane (real: 110.0 ± 5.6 nm, sim: 112.0 ± 5.6 nm, n
903 = 22,391 values/140 compartments/7 mice, $p < 0.001$, Chi-LRT).

904